REFERENCES AND NOTES

1. D. R. Ort *et al.*, *Proc. Natl. Acad. Sci. U.S.A.* **112**, 8529–8536 (2015).
2. Z. Li, S. Wakao, B. B. Fischer, K. K. Niyogi, *Annu. Rev. Plant Biol.* **60**, 239–260 (2009).
3. P. Müller, X.-P. Li, K. K. Niyogi, *Plant Physiol.* **125**, 1558–1566 (2001).
4. M. L. Pérez-Bueno, M. P. Johnson, A. Zia, A. V. Ruban, P. Horton, *FEBS Lett.* **582**, 1477–1482 (2008).
5. S. P. Long, S. Humphries, P. G. Falkowski, *Annu. Rev. Plant Biol.* **45**, 633–662 (1994).
6. C. Werner, R. J. Ryel, O. Correia, W. Beyschlag, *Plant Cell Environ.* **24**, 27–40 (2001).
7. X.-G. Zhu, D. R. Ort, J. Whitmarsh, S. P. Long, *J. Exp. Bot.* **55**, 1167–1175 (2004).
8. E. H. Murchie, K. K. Niyogi, *Plant Physiol.* **155**, 86–92 (2011).
9. C. D. P. Duffy, A. V. Ruban, *J. Photochem. Photobiol. B* **152** (pt. B), 215–226 (2015).
10. C. A. Wraight, A. R. Crofts, *Eur. J. Biochem.* **17**, 319–327 (1970).
11. M. D. Brooks, S. Jansson, K. K. Niyogi, in *Non-Photochemical Quenching and Energy Dissipation in Plants Algae and Cyanobacteria* (Springer, 2014), vol. 40, pp. 297–314.
12. M. Nilkens *et al.*, *Nature* **403**, 391–395 (2000).
13. B. Demmig-Adams, *Biochim. Biophys. Acta* **1020**, 1–24 (1990).
14. H. Y. Yamamoto, T. O. M. Nakayama, C. O. Chichester, *Arch. Biochem. Biophys.* **97**, 168–173 (1962).
15. S. Hubbart, O. O. Ajigboye, P. Horton, E. H. Murchie, *Plant J.* **71**, 402–412 (2012).
16. X.-P. Li, A. M. Gilmore, K. K. Niyogi, *J. Biol. Chem.* **277**, 33590–33597 (2002).
17. A. Zia, M. P. Johnson, A. V. Ruban, *Planta* **233**, 1253–1264 (2011).
18. X.-P. Li, P. Muller-Moule, A. M. Gilmore, K. K. Niyogi, *Proc. Natl. Acad. Sci. U.S.A.* **99**, 15222–15227 (2002).
19. B. Demmig-Adams, W. W. Adams III, *Planta* **198**, 460–470 (1996).
20. M. Nilkens *et al.*, *Biochim. Biophys. Acta* **1797**, 466–475 (2010).
21. M. P. Johnson, P. A. Davison, A. V. Ruban, P. Horton, *FEBS Lett.* **582**, 262–266 (2008).
22. A. V. Ruban, *Plant Physiol.* **170**, 1903–1916 (2016).
23. P. Horton, A. V. Ruban, R. G. Walters, *Annu. Rev. Plant Physiol. Plant Mol. Biol.* **47**, 655–684 (1996).
24. S. P. Long, X.-G. Zhu, S. L. Naidu, D. R. Ort, *Plant Cell Environ.* **29**, 315–330 (2006).
25. S.-H. Chang, R. C. Bugos, W.-H. Sun, H. Y. Yamamoto, *Photosynth. Res.* **64**, 95–103 (2000).
26. W.-H. Sun, A. S. Verhoeven, R. C. Bugos, H. Y. Yamamoto, *Photosynth. Res.* **67**, 41–50 (2001).
27. K. K. Niyogi, A. R. Grossman, O. Björkman, *Plant Cell* **10**, 1121–1134 (1998).
28. M. Havaux, L. Dall'osto, R. Bassi, *Plant Physiol.* **145**, 1506–1520 (2007).
29. N. Wang *et al.*, *Physiol. Plant.* **132**, 384–396 (2008).
30. D. R. Ort, S. P. Long, *Science* **344**, 484–485 (2014).
31. J. Kromdijk, S. P. Long, *Proc. Biol. Sci.* **283**, 20152578 (2016).
32. D. Tilman, M. Clark, *Daedalus* **144**, 8–23 (2015).

<div style="border:1px solid red">**REPORTS**</div>

SOLAR CELLS

Perovskite-perovskite tandem photovoltaics with optimized band gaps

Giles E. Eperon,[1,2]* Tomas Leijtens,[3]* Kevin A. Bush,[3] Rohit Prasanna,[3] Thomas Green,[1] Jacob Tse-Wei Wang,[1] David P. McMeekin,[1] George Volonakis,[4] Rebecca L. Milot,[1] Richard May,[2] Axel Palmstrom,[5] Daniel J. Slotcavage,[3] Rebecca A. Belisle,[3] Jay B. Patel,[1] Elizabeth S. Parrott,[1] Rebecca J. Sutton,[1] Wen Ma,[6] Farhad Moghadam,[6] Bert Conings,[1,7] Aslihan Babayigit,[1,7] Hans-Gerd Boyen,[7] Stacey Bent,[5] Feliciano Giustino,[4] Laura M. Herz,[1] Michael B. Johnston,[1] Michael D. McGehee,[2]† Henry J. Snaith[1]†

We demonstrate four- and two-terminal perovskite-perovskite tandem solar cells with ideally matched band gaps. We develop an infrared-absorbing 1.2–electron volt band-gap perovskite, $FA_{0.75}Cs_{0.25}Sn_{0.5}Pb_{0.5}I_3$, that can deliver 14.8% efficiency. By combining this material with a wider–band gap $FA_{0.83}Cs_{0.17}Pb(I_{0.5}Br_{0.5})_3$ material, we achieve monolithic two-terminal tandem efficiencies of 17.0% with >1.65-volt open-circuit voltage. We also make mechanically stacked four-terminal tandem cells and obtain 20.3% efficiency. Notably, we find that our infrared-absorbing perovskite cells exhibit excellent thermal and atmospheric stability, not previously achieved for Sn-based perovskites. This device architecture and materials set will enable "all-perovskite" thin-film solar cells to reach the highest efficiencies in the long term at the lowest costs.

Metal halide perovskites [ABX_3, where A is typically Cs, methylammonium (MA), or formamidinium (FA); B is Pb or Sn; and X is I, Br, or Cl] have emerged as an extremely promising photovoltaic (PV) technology owing to their rapidly increasing power conversion efficiencies (PCEs) and low processing costs. Single-junction perovskite devices have reached a certified 22% PCE (*1*), but the first commercial iterations of perovskite PVs will likely be as an "add-on" to silicon (Si) PVs. In a tandem configuration, a perovskite with a band gap of ~1.75 eV can enhance the efficiency of the silicon cell. (*2*) An all-perovskite tandem cell could deliver lower fabrication costs, but requires band gaps that have not yet been realized. The highest-efficiency tandem devices would require a rear cell with a band gap of 0.9 to 1.2 eV and a front cell with a band gap of 1.7 to 1.9 eV. Although materials such

as $FA_{0.83}Cs_{0.17}Pb(I_xBr_{1-x})_3$ deliver appropriate band gaps for the front cell (*2*), Pb-based materials cannot be tuned to below 1.48 eV for the rear cell. Completely replacing Pb with Sn can shift the band gap to ~1.3 eV (for $MASnI_3$) (*3*), but the tin-based materials are notoriously air sensitive and difficult to process, and PV devices based on them have been limited to ~6% PCE. (*3, 4*) An anomalous band-gap bowing in mixed tin-lead perovskite systems ($MAPb_{0.5}Sn_{0.5}I_3$) has given band gaps of ~1.2 eV but mediocre performance (~7% PCE). Very recently, PCE of >14% has been reported with $MA_{0.5}FA_{0.5}Pb_{0.75}Sn_{0.25}I_3$ cells, for band gaps >1.3 eV and all-perovskite four-terminal tandem cells with 19% efficiency (*5, 6, 7*). Here, we demonstrate a stable, 14.8% efficient perovskite solar cell based on a ~1.2-eV band gap $FA_{0.75}Cs_{0.25}Pb_{0.5}Sn_{0.5}I_3$ absorber. We measure open-circuit voltages (V_{oc}'s) of up to 0.83 V in these cells, which represents a smaller voltage deficit between band gap and V_{oc} than measured for the highest-efficiency lead-based perovskite cells. We then combined these with 1.8-eV $FA_{0.83}Cs_{0.17}Pb(I_{0.5}Br_{0.5})_3$ perovskite cells to demonstrate current-matched and efficient (17.0% PCE) monolithic all-perovskite two-terminal tandem solar cells on small areas and 13.8% PCE on large areas, with V_{oc} >1.65 V. Finally, we fabricated 20.3% efficient small-area and 16.0% efficient 1-cm^2 all-perovskite four-terminal tandems using a semitransparent 1.6-eV $FA_{0.83}Cs_{0.17}Pb(I_{0.83}Br_{0.17})_3$ front cell.

---

[1]Department of Physics, University of Oxford, Clarendon Laboratory, Parks Road, Oxford OX1 3PU, UK. [2]Department of Chemistry, University of Washington, Seattle, WA, USA. [3]Department of Materials Science, Stanford University, Lomita Mall, Stanford, CA, USA. [4]Department of Materials, University of Oxford, Parks Road, Oxford OX1 3PH, UK. [5]Department of Chemical Engineering, Stanford University, Via Ortega, Stanford, CA, USA. [6]SunPreme, Palomar Avenue, Sunnyvale, CA, USA. [7]Institute for Materials Research, Hasselt University, Diepenbeek, Belgium.
*These authors contributed equally to this work. †Corresponding author. Email: mmcgehee@stanford.edu (M.D.M.) and henry.snaith@physics.ox.ac.uk (H.J.S.)

Fig. 1. Tin-lead alloying. (**A**) Scanning electron micrographs showing the top surface of $FASn_xPb_{1-x}I_3$ films with different Sn percentages and $FA_{0.75}Cs_{0.25}Pb_{0.5}Sn_{0.5}I_3$ ("50% Sn, $FA_{0.75}Cs_{0.25}$"), fabricated by PAI deposition. The 0% Sn films were annealed at 170°C, and the other films were annealed at 70°C. (**B**) Plot of experimentally estimated band gap as a function of Sn percentage, determined from absorption onset in a Tauc plot (assuming direct band gap) of the absorption (black); PL peak positions are given in red. (**C**) Band gaps for Sn-Pb perovskite alloys calculated from first principles using a supercell containing eight BX_6 octahedra, where the Sn and Pb atoms are ordered relative to each other (see supplementary materials for full details). Points plotted represent all possible band gaps for a particular composition, based on all possible Sn-Pb configurations; a solid line is drawn through the lowest band-gap options as a comparison to experiment.
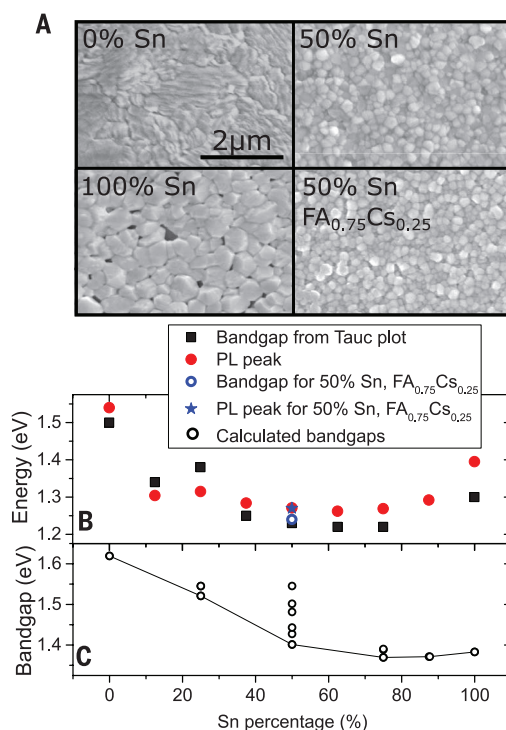
It has proved difficult to fabricate smooth, pinhole-free layers of tin-based perovskites on planar substrates (fig. S1) (*3*, *4*). We developed a technique, precursor-phase antisolvent immersion (PAI), to deposit uniform layers of tin-containing perovskites, $FASn_xPb_{1-x}I_3$, that combines two previous methods: the use of low–vapor pressure solvents to retard crystallization by forming precursor complexes and an antisolvent bath to crystallize the film with only gentle heating (*4*, *8*). Rather than using neat dimethyl sulfoxide (DMSO) as a solvent (*4*), a mixture of DMSO and dimethylformamide (DMF) allowed spin-coating of a uniform transparent precursor film that was not yet fully crystallized. Immersion of the films immediately in an antisolvent bath (anisole) (fig. S2) rapidly changed the film to a deep red. (*9*) Subsequent annealing at 70°C removed residual DMSO (fig. S7) to form smooth, dark, highly crystalline and uniform $FASn_xPb_{1-x}I_3$ films over the entire range of values of $x = 0$ to 1 (Fig. 1A). Only the neat Pb perovskite required heating at a higher temperature (170°C) to convert the film from the yellow room-temperature phase to the black phase (*10*).

Photoluminescence (PL) spectra and absorption spectra of a range of compositions (fig. S4)

allowed us to estimate the optical band gap from Tauc plots (from absorption, as discussed in the supplementary materials) and the PL peak positions (Fig. 1B) (*9*). The band gap narrowed between the two composition end points, similar to the observations of Kanatzidis *et al.* with the MA system (*5*), and between 50 and 75% Sn, was almost 1.2 eV. X-ray diffraction (XRD) spectra (fig. S5) for the whole series revealed a single dominant perovskite phase (table S1).

To understand this anomalous band-gap trend, we performed first-principles calculations of band gaps as a function of the tin-lead ratio (details in the supplementary materials) (*9*). For a disordered solid solution with Pb and Sn in random locations, the calculated band gap decreased monotonically (fig. S8). For an ordered structure, we placed the Sn and Pb atoms in specific positions relative to each other within a repeating lattice unit of eight octahedra in a "supercell." Here, if we take the lowest band gaps for each ratio, an anomalous band-gap trend emerges (Fig. 1C). For compositions with >50% Sn, a specific type of short-range order in the Pb-Sn positions allowed the band gap to dip below the end points. Im *et al.* attributed a similar band-gap trend observed for $MAPb_xSn_{1-x}I_3$

to the competition between spin-orbit coupling and distortions of the lattice (*11*), but if this was the case here, we should have observed it in the random solid solution approach. The energetic difference between the various Pb-Sn configurations was on the order of 2 meV, so at room temperature, the materials are likely to contain various combinations of the configurations that we show in fig. S7, but the absorption and emission onsets reflect the regions with the smallest gap.

To determine the charge-carrier diffusion length, mobility, and recombination lifetimes of these materials, we performed optical pump-probe terahertz (THz spectroscopy) on $FASnI_3$ and $FASn_{0.5}Pb_{0.5}I_3$. The fluence dependence of the THz transients for $FASn_{0.5}Pb_{0.5}I_3$ (fig. S9) exhibited faster decays at higher intensities as the result of increased bimolecular and Auger recombination (*12*). We calculated recombination rate constants and charge-carrier mobilities of 22 and 17 $cm^2 V^{-1} s^{-1}$ for $FASnI_3$ and $FASn_{0.5}Pb_{0.5}I_3$, respectively, comparable to values for Pb perovskite films (*12*, *13*). In comparison, for $MASnI_3$, the value was only 2 $cm^2 V^{-1} s^{-1}$ (*3*, *14*). For charge-carrier densities typical under solar illumination, charge-carrier diffusion lengths of ~300 nm were obtained for $FASn_{0.5}Pb_{0.5}I_3$ (details in the supplementary materials). Although lower than that for the best reported perovskite materials, it is equivalent to the typical thickness required to absorb most incident light (~300 to 400 nm) (*15*).

We fabricated a series of planar heterojunction devices in the "inverted" p-i-n architecture (*16*) comprising indium-tin-oxide (ITO)/poly(3,4-ethylenedioxythiophene)-poly(styrenesulfonate) (PEDOT:PSS)/$FASn_xPb_{1-x}I_3$/C_{60}/bathocuproine (BCP) capped with an Ag or Au electrode (Fig. 2A). The current density–voltage (*J-V*) curves and external quantum efficiency (EQE) measurements for the whole compositional series are shown in fig. S10. The onset of the EQEs closely matched that of the absorption of the materials, with light harvested out to ~1020 nm in the 50 to 75% Sn compositions. The highest efficiencies are generated from the devices with 50% Sn, within the lowest band-gap region; thus, we used this material to optimize our low-gap solar cells.

A small addition of Cs boosts the performance and stability of Pb-based perovskites (*17–19*). Substituting 25% of the FA with Cs in our films had little impact on band gap, morphology, PL, crystal structure, and charge carrier diffusion lengths (Fig. 1 and figs. S4 and S7), but device performance was enhanced (Fig. 2, B to D). The best $FASn_{0.5}Pb_{0.5}I_3$ device yields 10.9% PCE, whereas the best $FA_{0.75}Cs_{0.25}Sn_{0.5}Pb_{0.5}I_3$ device exhibited an impressive short-circuit current of 26.7 mA cm^{-2}, 0.74 V V_{oc}, and 0.71 fill factor (FF) to yield 14.1% PCE. The processing of each composition was optimized separately. These devices did not exhibit appreciable rate-dependent hysteresis, and the stabilized power output (14.8%) matched the scanned performance well. This efficiency was comparable with that of the best solution-processed low–band gap copper-indium-gallium-diselenide (CIGS) solar cells. (*20*) Thus, $FA_{0.75}Cs_{0.25}Pb_{0.5}Sn_{0.5}I_3$ is well

Table 1. Device parameters corresponding to the *J-V* curves in Fig. 2B.

	J_{SC} (mA cm^{-2})	V_{OC} (V)	FF	PCE (%)	SPO (%)
$FASn_{0.5}Pb_{0.5}I_3$	21.9	0.70	0.66	10.2	10.9
$FA_{0.75}Cs_{0.25}Sn_{0.5}Pb_{0.5}I_3$	26.7	0.74	0.71	14.1	14.8
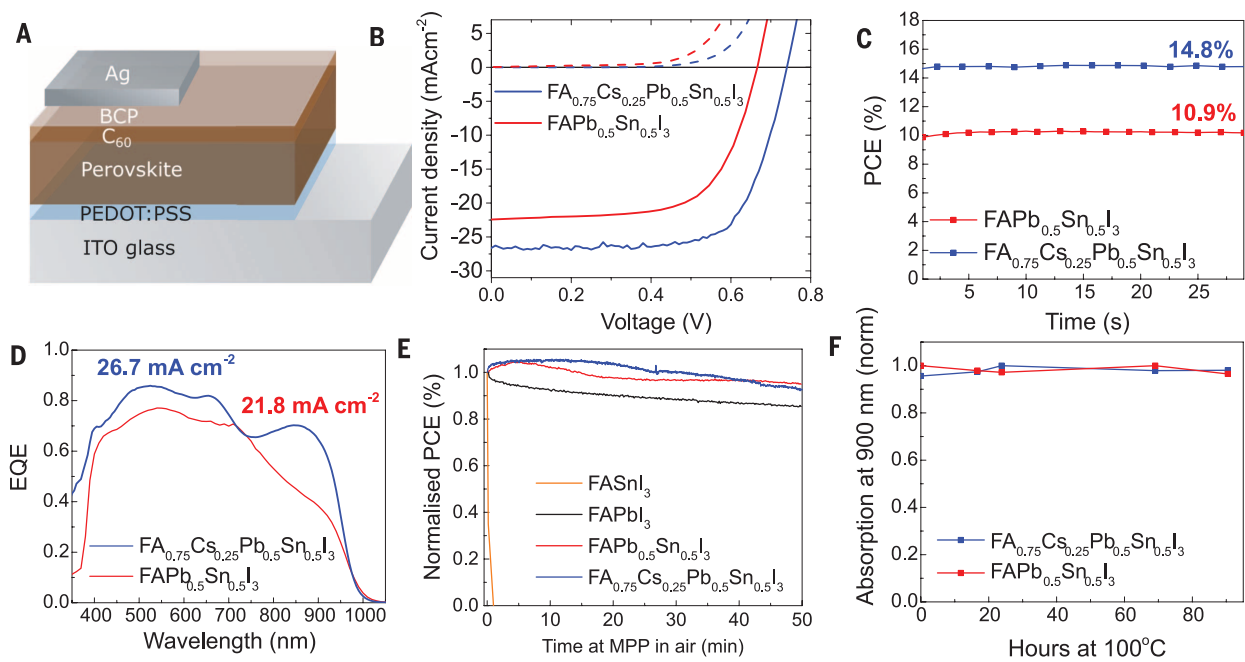
Fig. 2. Performance and stability of FASn$_{0.5}$Pb$_{0.5}$I$_3$ and FA$_{0.75}$Cs$_{0.25}$Sn$_{0.5}$Pb$_{0.5}$I$_3$ perovskite solar cells. (**A**) Schematic of the device architecture for narrow-gap single-junction perovskite solar cells. (**B**) Current-voltage characteristics under AM1.5G illumination for the best FASn$_{0.5}$Pb$_{0.5}$I$_3$ and FA$_{0.75}$Cs$_{0.25}$Sn$_{0.5}$Pb$_{0.5}$I$_3$ devices under illumination (solid lines) and in the dark (dashed lines), measured at 0.1 V/s with no prebiasing or light soaking. (**C**) Stabilized power output for the best solar cells, measured via a maximum power point tracking algorithm. (**D**) External quantum efficiency for the best devices of each material with the integrated current values shown providing a good match to the *J-V* scan *J*$_{sc}$. (**E**) PCE as a function of time for three compositions of FASn$_x$Pb$_{1-x}$I$_3$ (x = 0, 0.5, 1) as well as FA$_{0.75}$Cs$_{0.25}$Sn$_{0.5}$Pb$_{0.5}$I$_3$, measured by holding the cell at maximum power point in air under AM1.5G illumination. (**F**) Thermal stability of FASn$_{0.5}$Pb$_{0.5}$I$_3$ and FA$_{0.75}$Cs$_{0.25}$Sn$_{0.5}$Pb$_{0.5}$I$_3$ films, quantified by heating the samples at 100°C and monitoring their absorption at 900 nm as a function of time.
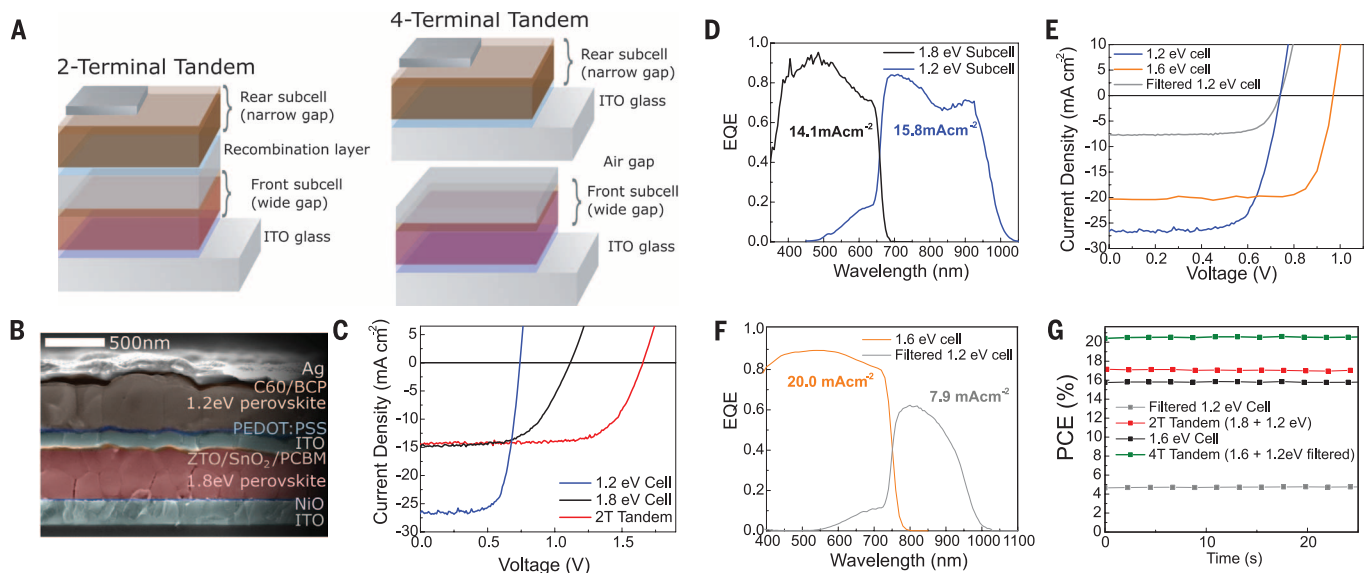

Fig. 3. Perovskite-perovskite tandems. (**A**) Schematics showing 2T and 4T tandem perovskite solar cell concepts. In this image, devices would be illuminated from below. (**B**) Scanning electron micrograph of the 2T perovskite-perovskite tandem. (**C**) Scanned current-voltage characteristics under AM 1.5G illumination, of the two-terminal perovskite-perovskite tandem, the 1.2-eV solar cell, and the ITO-capped 1.8-eV solar cell. (**D**) External quantum efficiency spectra for the subcells. (**E**) *J-V* curves of a 1.2-eV perovskite, of the same solar cell filtered by an ITO-capped 1.6-eV perovskite solar cell, and of the ITO-capped 1.6-eV perovskite solar cell, used to determine the mechanically stacked tandem efficiency. (**F**) External quantum efficiency spectra for the mechanically stacked tandem. (**G**) The stabilized power output tracked over time at maximum power point for the 2T perovskite solar cell, the 1.2-eV perovskite solar cell filtered by an ITO-capped 1.6-eV perovskite solar cell, the ITO-capped 1.6-eV perovskite solar cell, and the mechanically stacked tandem under AM1.5G illumination. The stabilized power output (SPO) for the 1.8-eV subcell is plotted in fig. S14 and given in Table 2.

Table 2. Solar cell performance parameters corresponding to the *J-V* curves shown in Fig. 3. Cell active areas are 0.20 or 1 cm². SPO, stabilized power output from maximum power point tracking. Large-area tandem data are plotted in fig. S19.

	J_{SC} (mA cm^{-2})	V_{OC} (V)	FF	PCE (%)	SPO (%)
1.2-eV cell	26.7	0.74	0.71	14.1	14.8
1.8-eV cell	15.1	1.12	0.58	9.8	9.5
2T tandem	14.5	1.66	0.70	16.9	17.0
Filtered 1.2-eV cell	7.9	0.74	0.73	4.4	4.5
ITO-capped 1.6-eV cell	20.3	0.97	0.79	15.7	15.8
4T tandem	–	–	–	20.1	20.3
1-cm² 2T tandem	13.5	1.76	0.56	13.3	13.8
1-cm² 4T tandem	–	–	–	16.4	16.0

suited for a rear junction in a solution-processed tandem solar cell, without the need for high-temperature thermal processing.

We performed ultraviolet photoelectron spectroscopy (UPS) and x-ray photoelectron spectroscopy (XPS) measurements to determine the energetic positions of the conduction and valence bands (fig. S11). The band levels for FASn$_{0.5}$Pb$_{0.5}$I$_3$ are well matched for C60 and PEDOT:PSS as electron and hole acceptors. The Cs-containing material showed an energetically shallower valance band and mild p-type doping (*21*, *22*).

The electronic losses in a solar cell are reflected by the difference in energy between the band gap of the absorber and V_{oc} (the loss in potential) (*23*). For crystalline silicon PV cells, which generate a record V_{oc} of 0.74 V and have a band gap of 1.12 eV, this loss is 0.38 V (*24*). Some of our FA$_{0.75}$Cs$_{0.25}$Sn$_{0.5}$Pb$_{0.5}$I$_3$ devices, with a thinner active layer, displayed V_{oc}'s up to 0.83 V (fig. S11), with a 1.24-eV band gap, exhibiting a comparable loss in potential of 0.41 eV.

Tin-based perovskites have previously been observed to be extremely unstable in air (*25*), so we carried out a simple aging test on the FASn$_{0.5}$Pb$_{0.5}$I$_3$ and FA$_{0.75}$Cs$_{0.25}$Pb$_{0.5}$Sn$_{0.5}$I$_3$ devices, comparing to FASnI$_3$ and FAPbI$_3$. We held the devices at maximum power point under 100 mW cm^{-2} illumination and measured power output over time in ambient air with a relative humidity of 50 ± 5% (Fig. 2E). The FAPbI$_3$ device maintained its performance relatively well, with a small drop observed over the time (to 85% of initial PCE over 50 min), possibly associated with photo-oxidation and hydration of the unencapsulated perovskite layer, or a partial reversion to the yellow room-temperature phase (*17*, *26*). Both the FASn$_{0.5}$Pb$_{0.5}$I$_3$ and FA$_{0.75}$Cs$_{0.25}$Sn$_{0.5}$Pb$_{0.5}$I$_3$ showed a stability similar to or even better than the neat Pb material. We also subjected bare perovskite films to thermal stress, heating for 4 days at 100°C under nitrogen; there were no changes in absorption spectra, a monitor of optical quality and hence stability (Fig. 2F) (*27*). We also monitored the performance of full devices at 85°C over

several months (fig. S13) and found that the Sn:Pb material displays device stability similar to that of the neat Pb material. The contribution of both Sn and Pb orbitals to the valence band minimum may reduce the propensity of Sn^{2+} to oxidize to Sn^{4+}.

A 1.2-eV perovskite is ideally suited as the rear cell in either monolithic two-terminal (2T) tandem solar cells or mechanically stacked four-terminal (4T) tandem solar cells (Fig. 3A). The subcells in a 2T tandem must be current matched to deliver optimum performance, and connected with a recombination layer. A 4T tandem operates the two cells independently but requires an extra transparent electrode, which can result in more absorption losses and higher cost. Theoretical efficiencies using a 1.2-eV rear cell (fig. S14) show that the 2T architecture requires the use of a top cell with a ~1.75- to 1.85-eV band gap, whereas the 4T architecture has a much more relaxed requirement of 1.6 to 1.9 eV.

We can obtain efficient and stable perovskites with appropriate wide band gaps for front cells in tandem architectures by using a mixture of FA and Cs cations (*2*) and control the band gap by tuning the Br:I ratio; FA$_{0.83}$Cs$_{0.17}$Pb(I$_{0.5}$Br$_{0.5}$)$_3$ has a 1.8-eV band gap that is ideally suited for the 2T tandem. However, their higher losses in potential compared with the more commonly used 1.6-eV perovskites (*28*) make the latter better suited for the 4T tandem. We prepared both of these perovskites in the p-i-n structure depicted in Fig. 3A, using NiO$_x$ and phenyl-C61-butyric acid methyl ester (PCBM) as the hole and electron contacts, respectively. We applied PAI deposition to form smooth and thick perovskite layers, obtaining efficient devices with appropriate photocurrents and voltages up to 1.1 V (see fig. S14) (*9*).

For the recombination layer in the 2T cell, we used layers of tin oxide and zinc-tin-oxide (ZTO) coated with sputter-coated ITO (*29*). This ITO layer completely protects the underlying perovskite solar cell from any solvent damage (fig. S16), meaning that we could fabricate the 1.2-eV

FA$_{0.75}$Cs$_{0.25}$Sn$_{0.5}$Pb$_{0.5}$I$_3$ solar cell directly on top. We plot the *J-V* curves of the best single-junction 1.2-eV cells and single-junction 1.8-eV cell, and that of the best 2T tandem device, in Fig. 3C. We observed good performance for the 2T tandem solar cells, exceeding either of the individual subcells despite the somewhat non-optimized 1.8-eV top cell. The photocurrent of the tandem solar cell was 14.5 mA cm^{-2}; voltage is an appropriate addition of the two subcells (1.66 V); and the fill factor is 0.70, yielding an overall performance of 16.9% via a scanned *J-V* curve and of 17.0% when stabilized at its maximum power point. None of the devices exhibit substantial hysteresis in the *J-V* curves (Fig. 3G and fig. S17).

The photocurrent is notably high when compared to the photocurrent density of the best reported monolithic perovskite-silicon tandems (*30*, *31*). External quantum efficiency (EQE) measurements (Fig. 3D) demonstrate that the two subcells are fairly well matched, with the wide-gap subcell limiting the current. One benefit of a tandem architecture, which we observe here, is that the FF tends not to be limited to the lowest value of the individual subcells, owing to the reduced impact of series resistance on a higher-voltage cell (*32*). Furthermore, we held a 2T tandem at its maximum power point under illumination in nitrogen for more than 18 hours, and it showed effectively no performance drop (fig. S18).

For a 4T tandem, we used an efficient 1.6-eV band gap FA$_{0.83}$Cs$_{0.17}$Pb(I$_{0.83}$Br$_{0.17}$)$_3$ perovskite, similar to that reported by McMeekin *et al.* but in p-i-n configuration (*2*) with a transparent ITO top contact. We obtained a 15.8% efficient solar cell with a V_{oc} ~1 V, and when we use it to filter a 14.8% FA$_{0.75}$Cs$_{0.25}$Sn$_{0.5}$Pb$_{0.5}$I$_3$ cell, we can still extract substantial photocurrent (7.9 mA cm^{-2}) from the low–band gap device. We plot the *J-V* curves and EQE spectra of the 1.6- and 1.2-eV cells in the 4T tandem in Fig. 3, E and F, and obtain an additional 4.5% PCE from the 1.2-eV rear cell, yielding an overall stabilized tandem efficiency of 20.3% (Fig. 3G).

The above results were for 0.2-cm² devices. We also made large-area (1 cm²) versions of the single junctions and 2T and 4T tandems. The current-voltage characteristics of these devices are shown in Table 2 and fig. S18, with 2T tandem 1-cm² devices exhibiting 13.8% stabilized PCE and 4T tandems 16.0%. The 17.0% PCE 2T and 20.3% 4T tandems, which are for devices that could be further optimized, already far exceed the best tandem solar cells made with other similarly low-cost semiconductors, such as those made with organic small molecules (world record is 13%) or amorphous and microcrystalline silicon (13.5%) (*1*, *24*). Notably, our results illustrate that the tandem cell should be at least 4 to 5% more efficient than the best 1.6-eV single-junction perovskite cells, indicating that as the efficiency of the single-junction cells increases, then the tandem approach will enable this low temperature–processed polycrystalline thin-film technology to surpass the 30% efficiency barrier.

REFERENCES AND NOTES

1. National Renewable Energy Laboratory, *Best Research-Cell Efficiencies*, www.nrel.gov/pv/assets/images/efficiency_chart.jpg (2016).
2. D. P. McMeekin *et al.*, *Science* **351**, 151–155 (2016).
3. N. K. Noel *et al.*, *Energy Environ. Sci.* **7**, 3061–3068 (2014).
4. F. Hao *et al.*, *J. Am. Chem. Soc.* **137**, 11445–11452 (2015).
5. F. Hao, C. C. Stoumpos, R. P. H. Chang, M. G. Kanatzidis, *J. Am. Chem. Soc.* **136**, 8094–8099 (2014).
6. L. Zhu *et al.*, *Nanoscale* **8**, 7621–7630 (2016).
7. Z. Yang *et al.*, *Adv. Mater.* 10.1002/adma.201602696 (2016).
8. Y. Zhou *et al.*, *J. Mater. Chem. A Mater. Energy Sustain.* **3**, 8178–8184 (2015).
9. See supplementary materials on *Science* Online.
10. C. C. Stoumpos, C. D. Malliakas, M. G. Kanatzidis, *Inorg. Chem.* **52**, 9019–9038 (2013).
11. J. Im, C. C. Stoumpos, H. Jin, A. J. Freeman, M. G. Kanatzidis, *J. Phys. Chem. Lett.* **6**, 3503–3509 (2015).
12. L. M. Herz, *Annu. Rev. Phys. Chem.* **67**, 65–89 (2016).
13. W. Rehman *et al.*, *Adv. Mater.* **27**, 7938–7944 (2015).
14. E. S. Parrott *et al.*, *J. Phys. Chem. Lett.* **7**, 1321–1326 (2016).
15. M. B. Johnston, L. M. Herz, *Acc. Chem. Res.* **49**, 146–154 (2016).
16. P. Docampo, J. M. Ball, M. Darwich, G. E. Eperon, H. J. Snaith, *Nat. Commun.* **4**, 2761 (2013).
17. Z. Li *et al.*, *Chem. Mater.* **28**, 284–292 (2016).
18. J.-W. Lee *et al.*, *Adv. Energy Mater.* **5**, 1501310 (2015).
19. C. Yi *et al.*, *Energy Environ. Sci.* **9**, 656–662 (2016).
20. T. K. Todorov, O. Gunawan, T. Gokmen, D. B. Mitzi, *Prog. Photovolt. Res. Appl.* **21**, 82–87 (2013).
21. P. Schulz *et al.*, *Energy Environ. Sci.* **7**, 1377–1381 (2014).
22. C. Wang *et al.*, *Appl. Phys. Lett.* **106**, 111603 (2015).
23. H. J. Snaith, *Adv. Funct. Mater.* **20**, 13–19 (2010).
24. M. A. Green, K. Emery, Y. Hishikawa, W. Warta, E. D. Dunlop, *Prog. Photovolt. Res. Appl.* **23**, 1–9 (2015).
25. F. Hao, C. C. Stoumpos, D. H. Cao, R. P. H. Chang, M. G. Kanatzidis, *Nat. Photonics* **8**, 489–494 (2014).
26. T. Leijtens *et al.*, *Adv. Energy Mater.* **5**, 1500963 (2015).
27. B. Conings *et al.*, *Adv. Energy Mater.* **5**, 1500477 (2015).
28. M. Saliba *et al.*, *Science* **354**, 206–209 (2016).
29. K. A. Bush *et al.*, *Adv. Mater.* **28**, 3937–3943 (2016).
30. J. Werner *et al.*, *J. Phys. Chem. Lett.* **7**, 161–166 (2016).
31. S. Albrecht *et al.*, *Energy Environ. Sci.* **9**, 81–88 (2015).
32. A. Hadipour *et al.*, *Adv. Funct. Mater.* **16**, 1897–1903 (2006).

ORGANIC CHEMISTRY

Asymmetric synthesis of batrachotoxin: Enantiomeric toxins show functional divergence against Na_V

Matthew M. Logan,* **Tatsuya Toma,†** **Rhiannon Thomas-Tran,‡** **J. Du Bois§**

The steroidal neurotoxin (−)-batrachotoxin functions as a potent agonist of voltage-gated sodium ion channels (Na_Vs). Here we report concise asymmetric syntheses of the natural (−) and non-natural (+) antipodes of batrachotoxin, as well both enantiomers of a C-20 benzoate–modified derivative. Electrophysiological characterization of these molecules against Na_V subtypes establishes the non-natural toxin enantiomer as a reversible antagonist of channel function, markedly different in activity from (−)-batrachotoxin. Protein mutagenesis experiments implicate a shared binding side for the enantiomers in the inner pore cavity of Na_V. These findings motivate and enable subsequent studies aimed at revealing how small molecules that target the channel inner pore modulate Na_V dynamics.

The phenotypic effects of acute poisons found among the rich pharmacopeia of terrestrial and marine life have been documented from antiquity. Isolation and characterization of toxic compounds have made available important chemical reagents for studying complex biochemical circuits (*1*). Studies of this type have revealed a large number of peptide and small-molecule agents that target voltage-gated sodium ion channels (Na_Vs), an obligatory class of membrane proteins for bioelectrical signaling (*1–4*). Among the collection of known Na_V modulators are three structurally related agents, (−)-batrachotoxin [(−)-BTX], veratridine, and aconitine (Fig. 1A)—sterically large, lipophilic amine derivatives believed to share a common binding locus in the inner pore region of Na_V (*3*) (site 2, Fig. 1B). The influence of these toxins on ion gating, however, differs distinctly. On one extreme, (−)-BTX, the primary toxic constituent of Colombian poison dart frogs (genus *Phyllobates*), is a full Na_V agonist, causing the channel to open more readily at hyperpolarized membrane potentials and blocking fast inactivation (among other characteristic effects) (*3–5*). Conversely, the activities of veratridine and aconitine are best described as partial agonism and inhibition of channel function, respectively (*5*). Despite recent insights from structural biology into the three-dimensional architecture of prokaryotic Na_Vs (*6–9*), a molecular understanding of the influence of the site 2 toxins on ion conduction and ion gating kinetics is lacking. Toxin structure-activity studies, in combination with protein mutagenesis experiments, can address questions related to the dynamical nature of channel function and may guide the rational design of

small-molecule modulators of Na_V activity (*1*). The potency of (−)-BTX (*10*), its storied history as the archetypal small-molecule site 2 probe (*4*), and its unparalleled effects on channel gating render it an optimal "lead" compound for such investigations.

(−)-BTX binding to Na_Vs alters every aspect of channel function, resulting in a hyperpolarized shift in the voltage dependence of activation, inhibition of both fast and slow inactivation, a decrease in single-channel conductance, and reduction of ion selectivity (*3*, *4*). The utility of this natural product as a Na_V activator has led to a substantial depletion in the world supply, which once exceeded 1 g but was less than 170 mg as of 2009 (*11*, *12*). Since the toxin was first isolated in 1963 by Märki and Witkop from poisonous frogs collected in the northern rain forest of Colombia (*13*), *Phyllobates* has been placed on the endangered species list, and thus collection of natural (−)-BTX from this source is restricted. (−)-BTX has also been identified in select species of birds (genus *Pitohui* and *Ifrita*) (*14*) and beetles (genus *Choresine*) (*15*), but only in small quantities (e.g., ~1.8 µg of (−)-BTX per beetle). Although semi- (*16*) and racemic syntheses (*17*) of BTX-A (Fig. 1C), a compound lacking the C-20 pyrrole ester, have been disclosed, the length of each of these works (>45 linear steps) precludes the facile production of (−)-BTX or select analogs. Accordingly, our desire to use BTX and modified forms thereof for examining channel dynamics and ion gating mechanisms has motivated our efforts to obtain the natural product through de novo synthesis.

Retrosynthetic analysis of (−)-BTX led us to outline a plan that would enable late-stage assembly of the homomorpholine E ring and elaboration of the C-20 allylic ester (Fig. 1C), thereby facilitating access to modified forms of the toxin. Previous structure-activity relationship studies using a small number of semisynthetic BTX derivatives (*10*, *18*) and C/D/E-ring BTX analogs (*19*) revealed the importance of the C-20 ester, tertiary amine, and tetracyclic skeleton for Na_V

Department of Chemistry, Stanford University, Stanford, CA 94305-5080, USA.
*Present address: Gilead Sciences, Foster City, CA 94404, USA.
†Present address: Graduate School of Pharmaceutical Sciences, Nagoya University, Furo-cho, Chikusa-ku, Nagoya 464-8601, Japan.
‡Present address: Arcus Biosciences, Hayward, CA 94545, USA.
§Corresponding author. Email: jdubois@stanford.edu